Mechanical Systems and Signal Processing 213 (2024) 111336

Contents lists available at ScienceDirect

Mechanical Systems and Signal Processing

journal homepage: www.elsevier.com/locate/ymssp

Mode-shape magnification in high-speed camera measurements

Krištof Čufar [a,b], Janko Slavič [a,*], Miha Boltežar [a]

[a] *University of Ljubljana, Faculty of Mechanical Engineering, Aškerčeva 6, 1000 Ljubljana, Slovenia*
[b] *Domel, d.o.o. Otoki 21, 4228 Železniki, Slovenia*

ARTICLE INFO

Communicated by J.E. Mottershead

Keywords:
Image-based structural identification
Mode-shape magnification
Motion magnification
DIC
Optical flow

ABSTRACT

If motion, identified using image-based methods, is too small to be seen with the naked eye, motion magnification can be used to help with the visualization. Established motion-magnification methods magnify (typically up to 1000 times) the band-passed content of the image data. Especially at higher frequencies, the amplitudes of measured displacements are often below the noise floor. In this research, a novel method for amplifying vibrations, based on experimental modal analysis (EMA), is introduced. The response of the examined structure to dynamic excitation is measured with a simplified, gradient-based, optical flow method and used to perform a hybrid modal analysis in conjunction with a reference accelerometer response measurement. Such a hybrid approach can: (a) identify structural dynamics significantly in the sub-pixel range, and (b) significantly below the image noise floor. The image of the vibrating structure is subdivided using a planar triangle mesh, which is then warped in accordance with the identified mode shape. A mesh-element-wise affine transformation is performed to obtain an image of the magnified mode shape. In the experimental part, the proposed method achieved magnification factors of approximately 40 thousand times, which is an order of magnitude deeper into noise than available before; additionally, the proposed approach is numerically significantly less demanding.

The introduced mode-shape magnification presents an alternative to existing motion-magnification methods for applications where the harmonic displacement information is hidden by image noise.

1. Introduction

Image-based methods for measuring displacements are becoming a viable, non-contact, full-field alternative to conventional measurement techniques in the field of structural dynamics [1,2]. Displacements that are invisible to the naked eye can be measured and serve as a basis for accurate modal identification [3,4]. A closely related area of research is the visualization of magnified full-field mode shapes; however, current methods can lead to inaccurate results and artifacts [5,6].

Some of the earlier attempts to apply image-based displacement-identification methods to the field of structural dynamics identification were based on the point-tracking (PT) approach [7]. In 2002, Ryall et al. [8] proposed a single-camera 3D PT method. Around 2010, the 3D digital image correlation (DIC) method was used to measure the deflection shapes of thin structures vibrating with resonant frequencies [9,10]. A comparison of 3D DIC to the more conventional laser-Doppler-vibrometry approach to measuring 3D deflection shapes can be found in [2,11], while Baqersad et al. [12] provided a review of image-based methods used in the field of structural dynamics. Alternatively, gradient-based displacement-identification methods [13] have been used for vibration measurements. In 2017 Javh et al. [3,4] proposed a simplified optical method with a resolution potential deep in the sub-pixel

---

[*] Corresponding author.
E-mail address: janko.slavic@fs.uni-lj.si (J. Slavič).

https://doi.org/10.1016/j.ymssp.2024.111336
Received 24 January 2024; Accepted 9 March 2024

territory. As high-speed cameras are still an expensive technology, efforts have been made to manage the cost of image-based vibration measurements. In 2018 Javh et al. [14] proposed a spectral optical flow imaging (SOFI) method that enabled high-frequency modal identification using only a DSLR camera and in 2019 Gorjup et al. [15] showed that 3D operating deflection shapes can be determined using a single high-speed camera and triangulation in the frequency domain. In 2020 Khadka et al. [16] applied DIC and PT methods to measure vibrations of rotating wind turbine blades using a stereo-camera set-up attached to an UAV. In 2023, Gardonio et al. [17] extracted 3D deflection shapes of a thin plate using 3D PT and used them to reconstruct the sound radiation, and Hu et al. [18] used PT displacement measurements as a basis for their method of damage detection on bridges. Atashipour et al. proposed a method of identifying directionally-dependent elastic properties of skin based on full-field 3D DIC measurements [19]. Phase-based motion estimation has also become a popular method for structural dynamics identification [5,20,21]. In 2024, Merainani et al. [22] extended the phase-based motion-estimation approach to super-pixel displacements and combined it with a subspace identification approach to perform operational modal analysis on a cantilever beam.

In structural dynamics the displacements of interest are usually too small to be visible from the raw video with the naked eye. Motion magnification was first introduced by Liu et al. [23] in 2005 as a technique for the visualization of small displacements. Magnification factors of up to 80 were used in this work. In the first motion-magnification methods the displacements were explicitly determined and used to warp the image [23,24]. These methods were termed Lagrangian, as the motion of each point was determined separately. Alternatively, Eulerian methods, first introduced in 2013 [25,26], employ spatio-temporal video decomposition to extract and amplify the signals of interest. Wadhwa et al. [26] cited magnification factors of 150. In 2015, Chen et al. [5] used the phase-based Eulerian motion-magnification approach to visualize the operating deflection shapes (ODS) of structures using magnification factors of up to 400, and in 2018 Molina-Viedma et al. [27] extended this approach with DIC-based contour plots to visualize the high-frequency ODS of a cantilever beam. In 2017, Poozesh et al. [28] used phase-based motion magnification (PMM) to improve the signal-to-noise ratio (SNR) before identifying the displacements using 3D DIC and 3D PT, while in 2022 Valente et al. [29] quantified the ODS of a cantilever beam by applying a PT algorithm to a phase-based motion-magnified video. PMM has also been used to identify defects on thin plates [30]. Luo et al. introduced a method for performing PMM on a broad frequency band [31]. It has been noted that PMM methods, which are currently most commonly used among motion-magnification methods, do not necessarily produce physically accurate results [5,6].

Efforts have been made to perform accurate modal analysis based on image-based vibration measurements. In 2012, Wang et al. [32] performed modal identification by applying a non-linear, least-squares, curve-fitting approach to shape descriptor frequency-response functions (FRFs). In 2017, Yang et al. [33] proposed a method for operational modal analysis using phase-based estimated motion. A year later, Javh et al. [4] introduced the hybrid method, combining the high dynamic range of conventional vibration-measurement techniques with the full-field capabilities of optical methods. In 2021, Bregar et al. [34] extended this method with a dynamic substructuring technique to improve the quality of the reconstructed FRF at higher frequencies. In 2022, Wang et al. [35] used the PolyMAX method [36] in conjunction with random sampling to perform EMA above the Nyquist frequency of the high-speed-camera measurement. Morlet-wave-based damping identification has also been performed on image-based identified displacements [37]. Cao et al. [38] conducted an operational modal analysis by first extracting the resonant frequencies using a frequency-domain decomposition and then estimating the mode shapes with infinite impulse-response filters at these frequencies. In 2023 Willems et al. [39] exploited the high spatial density of image-based vibration measurements to identify the structural dynamics of a thin plate in the time domain. Lo Feudo et al. employed Kalman filtering to perform modal analysis of nonlinear systems [40].

The aim of the mode-shape magnification method introduced in the present work is to accurately visualize the mode shapes of structures obtained via reliable modal identification methods. Synchronized measurement of the excitation and response of the examined structure is performed first. The response is measured using an image-based method along with a conventional vibration sensor (*e.g.* accelerometer). The mode shapes of the structure are identified in a scarce set of points using the hybrid modal identification method [4]. The image of the structure is descretized by a triangle mesh based on this set of points. The mesh is warped in accordance with a given scaled mode shape and the image areas of each mesh element are transformed using an element-wise affine transformation.

This manuscript is organized as follows. The theoretical background that is the basis of this scientific article is presented in Section 2. The mode-shape magnification method is introduced in Section 3 and an experimental demonstration is given in Section 4. The conclusions are drawn in Section 5.

2. Theoretical background

2.1. Simplified optical flow displacement identification

In this research the displacements are identified from a high-speed camera video using the simplified gradient-based optical flow (SGBOF) method introduced by Javh et al. [3]. Here, a short theoretical background is presented, for details please see [3,15]. The mode-shape magnification method introduced later is not limited to the SGBOF method (*e.g.*, digital image correlation (DIC) methods could be used instead).

The high-speed-camera measurement results in an array of gray-scale images. Each image is stored in the form of a 2D matrix, representing a discrete image-intensity function $I(x, y)$, where x and y are the pixel coordinates. It is assumed that the reflectivity pattern of the object and the illumination of the scene are constant. Consequently, the change of image intensity when the object in focus is in motion is given by [41]:

$$I(x_j, y_k, t) = I(x_j + \Delta x, y_k + \Delta y, t + \Delta t), \tag{1}$$

where the displacements in the x and y directions are Δx and Δy, respectively. Δt is the time step between the images while x_j and y_k are the pixel coordinates. If a stationary camera is assumed, the image-intensity function $I(x, y, t)$ is time dependent only because of the displacement of the observed object. In structural dynamics, both the time step between two images and the expected displacements can be assumed to be relatively small. Usually, sub-pixel displacements are expected [3]. The image-intensity function can therefore be approximated with a Taylor series, truncated after the linear terms [3] and the optical flow equation is subsequently derived from Eq. (1) [13,41]:

$$\frac{\partial I}{\partial x}\Delta x + \frac{\partial I}{\partial y}\Delta y + \frac{\partial I}{\partial t}\Delta t = 0 \tag{2}$$

For an observed pixel, the change in image intensity between sequential images is given by the term $\partial I/\partial t \Delta t$, and the gradients $\partial I/\partial x$ and $\partial I/\partial y$ can also be calculated, as the image-intensity function $I(x, y, t)$ is known. Since Eq. (2) cannot be solved for two unknowns Δx and Δy, the SGBOF method computes the displacements in the direction of the image-intensity gradient s [3]:

$$s(x_j, y_k, t) = \frac{I_0(x_j, y_k) - I(x_j, y_k, t)}{|\nabla I_0|} \tag{3}$$

The observed displacements are expected to be sub-pixel in magnitude and moving in the range of a constant image-intensity gradient, so the entire displacement time series can be calculated based on an initial or reference image I_0. The intensity gradient's magnitude is given by:

$$|\nabla I_0| = \sqrt{\left(\frac{\partial I}{\partial x}\right)^2 + \left(\frac{\partial I}{\partial y}\right)^2} \tag{4}$$

A single image can be used as the reference I_0, although for sub-pixel motion the usual approach is to temporally average a set of n_{avg} images from the start of the measurement with the aim of reducing the noise in the image [3]:

$$I_0 = \frac{1}{n_{avg}} \sum_{i=1}^{n_{avg}} I_i \tag{5}$$

2.2. Hybrid modal-parameter-estimation method

The displacement measurements obtained with high-speed cameras are usually contaminated with relatively high noise levels, which makes modal parameter estimation difficult [4]. The hybrid method introduced by Javh et al. [4] combines the high dynamic range of conventional accelerometer measurements with the full-field capabilities of high-speed cameras. Recently, Zaletelj et al. [42] used the hybrid method in the field of model updating.

The eigenvalues of the observed structure are first identified by applying the Least-Squares Complex Frequency (LSCF) method introduced by Guillaume et al. [43] to the high-dynamic-range sensor (*e.g.* accelerometer) measurement data to identify the eigenvalues of the structure.

The frequency response function (FRF) is modeled using the common denominator model (CDM) [44]:

$$\alpha_j(\omega) = \frac{\sum_{r=0}^{2N} a_{j,r}\, e^{-\mathrm{i}\, r\, \Delta t\, \omega}}{\sum_{r=0}^{2N} b_r\, e^{-\mathrm{i}\, r\, \Delta t\, \omega}}, \tag{6}$$

where j is the output measurement location of a Single-Input-Multiple-Output measurement and the input measurement's location index is omitted. r is the polynomial order and N is the number of considered modes. $a_{j,r}$ and b_r are the unknown numerator and denominator polynomial roots, while Δt is the time step in seconds and ω is the angular frequency in radians per second.

The accelerometer measurement based FRF $\alpha_j(\omega)$ is inserted into Eq. (6) and the numerator coefficients $a_{j,r}$ are eliminated from the system [43]. The denominator roots b_r (that are also the poles of the function) are first estimated for increasing polynomial orders. A stabilization chart is then constructed and the physically meaningful poles can be selected, as they remain stable with the increasing polynomial order. The selected poles correspond to the complex eigenvalues of the observed structure λ_r:

$$\lambda_r = -\zeta_r\, \omega_r \pm \mathrm{i}\, \omega_r \sqrt{1 - \zeta_r^2} \tag{7}$$

from which the natural frequencies ω_r and damping ratios ζ_r can be extracted.

The numerator roots that govern the modal constants ${}_rA_{ij}$ and consequently the eigenvectors ϕ_r of the system can then be calculated [43]. In the hybrid method [4] this step is omitted however and the modal constants are identified from the high-speed-camera measurements using the Least-Squares Frequency Domain (LSFD) method [45]. This time, the FRF $\alpha_j(\omega)$ is defined as:

$$\alpha_j(\omega) = \sum_{r=1}^{N} \left(\frac{{}_rA_j}{\mathrm{i}\,\omega - \lambda_r} + \frac{{}_rA_j^*}{\mathrm{i}\,\omega - \lambda_r^*} \right) - \frac{A_L}{\omega^2} + A_U \tag{8}$$

A_L and A_U are the lower and upper residuals, respectively. Eigenvalues λ_r from the accelerometer data are used and the mode shapes are obtained for all the response-measurement points of the camera data set j.

Each frequency point of the high-speed-camera-estimated FRF $\alpha_j(\omega)$ is used in Eq. (8) to produce an overdetermined system of linear equations, from which the modal constants can be estimated [4].

2.3. Planar mesh generation

To produce an image of a magnified mode shape, the input image of the observed structure needs to be warped. Based on the measured locations (index j in Eq. (8)) a triangle mesh is created. Then, the mesh and the image are warped in accordance with the identified mode shapes.

The Delaunay triangulation methods are the most commonly used to produce the two-dimensional, unstructured, triangle mesh based on a set of co-planar points [46]. These methods are based on the Delaunay criterion [47]. In two dimensions the criterion states that no node of the mesh can be contained inside the circumcircle of any of the triangle elements.

The Delaunay triangulation is frequently used because it maximizes the minimal angle of the triangle mesh elements [48], resulting in a better aspect ratio. In this work a randomized, incremental algorithm based on the work of Guibas et al. [49] is used [50,51]. For an in-depth explanation of the Delaunay triangulation, the reader is referred to [48].

2.4. Affine image transformation

If the mesh overlaying the image is changed, the image can be distorted using an affine image transformation to match the mesh. An affine image transformation is a geometric image transformation generally comprised of translation, rotation, scaling and shearing [52]. In homogeneous coordinates it is defined by [52]:

$$\begin{Bmatrix} x' \\ y' \\ 1 \end{Bmatrix} = \mathbf{A} \begin{Bmatrix} x \\ y \\ 1 \end{Bmatrix} = \begin{bmatrix} a_{11} & a_{12} & a_{13} \\ a_{21} & a_{22} & a_{23} \\ 0 & 0 & 1 \end{bmatrix} \begin{Bmatrix} x \\ y \\ 1 \end{Bmatrix} \tag{9}$$

where $\mathbf{A}$ is the affine transformation matrix, (x', y') are the coordinates of a point in the transformed image and (x, y) are the original image-point coordinates.

The elements of matrix $\mathbf{A}$ are uniquely defined using the 3 points with known coordinates (x'_i, y'_i) and (x_i, y_i). Using $i = 1, 2, 3$ the system of linear equations is:

$$\begin{bmatrix} x_1 & y_1 & 1 & 0 & 0 & 0 \\ 0 & 0 & 0 & x_1 & y_1 & 1 \\ x_2 & y_2 & 1 & 0 & 0 & 0 \\ 0 & 0 & 0 & x_2 & y_2 & 1 \\ x_3 & y_3 & 1 & 0 & 0 & 0 \\ 0 & 0 & 0 & x_3 & y_3 & 1 \end{bmatrix} \begin{Bmatrix} a_{11} \\ a_{12} \\ a_{13} \\ a_{21} \\ a_{22} \\ a_{23} \end{Bmatrix} = \begin{Bmatrix} x'_1 \\ y'_1 \\ x'_2 \\ y'_2 \\ x'_3 \\ y'_3 \end{Bmatrix} \tag{10}$$

Since the transformed coordinates generally do not coincide with the regular grid of the original image, interpolation is needed to determine the image-intensity value of the pixel in its transformed location [52]. In the case of using the inverse mapping approach, the corresponding locations in the original image (x_i, y_i) are calculated for each location in the transformed image (x'_i, y'_i) using the inverse affine transformation. The image-intensity value is then determined by interpolating the values of the closest pixels in the input image [52].

3. Mode-shape magnification in high-speed camera measurements

The objective of the proposed method is to produce a mode-shape magnified image. The key steps to obtaining this result are:

1. Subset selection and displacement identification using the SGBOF method (Section 2.1)
2. Hybrid method experimental modal analysis (EMA) (Section 2.2)
3. Planar mesh creation (Section 2.3)
4. Image transformation (Section 2.4)

Details of key steps are given in the following subsections, for open-source implementation as introduced in this manuscript, please see the Python package pyIDI [53].

3.1. Subset selection and displacement identification

Using the SGBOF method, motion can be evaluated in every pixel; however as will be discussed later, not every pixel can result in reliable measurement information. In this section, the SGBOF method, as introduced in [3], is expanded to two dimensional motion estimation by means of a subset-based approach.

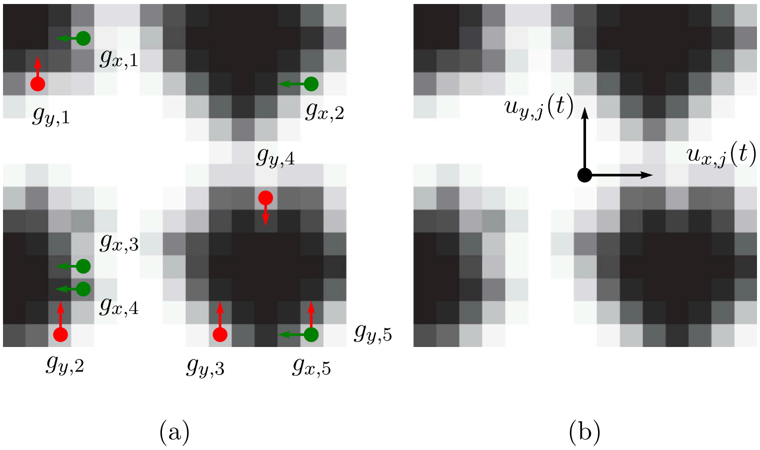

Fig. 1. Displacement identification for a 15×15 subset, $n_x = n_y = 5$ (a) Selected pixels with the highest gradient in the x and y directions (b) Calculated displacements attributed to the central pixel.

First, a selection of pixels, where the displacements will be identified, is made based on the local image-intensity gradients. The reference image I_0 is obtained using Eq. (5) and the intensity gradients $\partial I_0/\partial x$ and $\partial I_0/\partial y$ are then calculated along with the intensity-gradient magnitude (4). The reference image is then divided into square subsets of size $(2m+1) \times (2m+1)$, where m is a positive integer. For each subset n_x and n_y pixels with the highest intensity gradient in the x and y directions respectively are selected (Fig. 1(a)).

Only subsets where the gradients of all n_x and n_y pixels are higher than the pre-set limits ($g_{x,\min}$, $g_{y,\min}$, respectively) are selected for further consideration:

$$\min\left[\left(\frac{\partial I_0}{\partial x}\right)_j\right] > g_{x,\min} \wedge \min\left[\left(\frac{\partial I_0}{\partial y}\right)_j\right] > g_{y,\min} \tag{11}$$

The central pixels of the subsets will later serve as nodes of the triangle mesh. Using the SGBOF method (3) the displacements within the subset are evaluated at the selected n_x and n_y pixels, only. The x and y components of the displacements are investigated separately.

Since the subsets are relatively small, it can be assumed that there is no relative motion between the points inside a subset. Consequently, the displacement in the x direction can be averaged over the subset:

$$s_{x,avg,j}(t) = \frac{1}{n_x}\sum_{k=1}^{n_x} s_{x,j,k}(t), \tag{12}$$

where j denotes the currently observed subset and $k = 1, \dots, n_x$ are the selected subset pixels. Analogously, the average y component of the subset displacement is obtained and both components are attributed to the central pixel of the subset (Fig. 1(b)).

Smaller subsets can be used to obtain a higher spatial resolution for the resulting displacement information or larger subsets can be chosen to further reduce the effect of the noise.

The intensity-gradient threshold of Eq. (11) can also be used to differentiate the observed object from the background. It is assumed that a speckle pattern has been applied to the object and that the depth of field for the measurement has been set so that the background is blurred. Consequently, the average intensity gradient is expected to be higher in the subsections depicting the observed object. This approach also filters out areas of the object that are poorly lit or lack an adequate speckle pattern. The segmentation is demonstrated in Fig. 2, where the blue dots represent the central pixels of the remaining subsets after using Eq. (11).

When larger subsets are employed, a problem of bias may arise, if most of the selected pixels are gathered towards one side of the subset. To overcome this problem, the average displacement may be attributed to the center of the used pixels, instead of the center of the subset (Fig. 1(b)).

3.2. Hybrid experimental modal analysis

The displacements are measured with the high-speed camera and the obtained FRF is in the form of receptance $\alpha(\omega)$, while the accelerometers produce a measurement in the form of accelerance $A(\omega)$. Before the hybrid experimental modal analysis is performed, the accelerometer-data-based FRF is transformed to receptance [54]:

$$\alpha(\omega) = -\frac{1}{\omega^2} A(\omega) \tag{13}$$

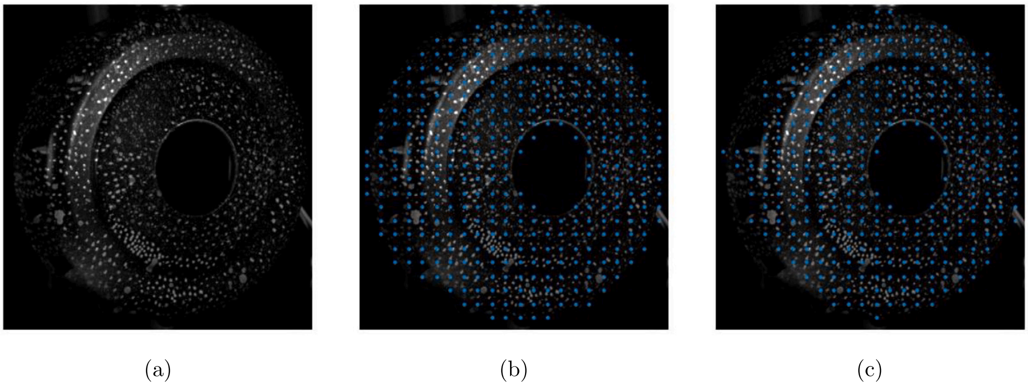
(a) (b) (c)

Fig. 2. Effect of gradient limits $g_{x,\min}$ and $g_{y,\min}$. (a) The input image (b) No limit is set (c) $g_{x,\min} = g_{y,\min} = 4000$.

The eigenvalues of the observed system are then obtained by applying the LSCF method (6) to the reference accelerometer measurements. Then, two separate LSFD analyses are carried out for the x and y displacement data obtained from the high-speed-camera measurements to produce the x and y components of the mode shapes, $\phi_{x,r}$ and $\phi_{y,r}$. The jth subset (12) is now represented by the mode-shape elements $\phi_{x,j,r}$ and $\phi_{y,j,r}$.

3.3. Planar mesh creation

In the final part of the method, a triangle mesh is created. The nodes of the mesh correspond to the central pixels of the subsets j (12), where the mode shapes are defined. The reference image I_0 is warped mesh-element-wise using the affine transformation (9) in accordance to the scalar multiplied mode shapes (14).

The mesh is warped by translating the nodes:

$$\begin{Bmatrix} x'_j \\ y'_j \end{Bmatrix} = \begin{Bmatrix} x_j + \phi_{x,j,r} \cdot c \\ y_j + \phi_{y,j,r} \cdot c \end{Bmatrix} \tag{14}$$

where (x_j, y_j) and (x'_j, y'_j) are the node coordinates in the original and deformed mesh respectively and $\phi_{x,j,r}$ is the element of the rth x component mode shape corresponding to the jth subset. The magnification of the mode shape is set by changing the scale factor c.

The construction of the triangle mesh is automated to a great degree thanks to the employment of the well established Delaunay triangulation in combination with the subset based displacement identification, described in Section 3.1.

3.4. Image warping

The original and deformed node locations of each mesh element are used to produce affine transformation matrices (10). A region defined by each original mesh element is cropped out from I_0 and transformed using Eq. (9). The transformed region is then inserted at the location of the corresponding deformed mesh element.

Fig. 3 provides a block diagram of the proposed method. First, the vibration excitation and response data is obtained experimentally. Next, the images of the high-speed camera video are processed using the simplified gradient-based optical flow (SGBOF) method to obtain the displacements. The measurements are then transformed to the frequency domain using the Fast Fourier Transform (FFT). The hybrid modal analysis is performed and mode shapes with high spatial density φ_r are identified. Finally, the warping of the image is performed in four steps. Firstly, a triangle mesh is generated over the original image. Secondly, the mesh is warped in accordance with the mode shape φ_r and the scaling factor α. The affine transformation is then performed on each triangle element of the mesh based on the known locations of its nodes. Lastly, the transformed triangles are assembled into the output image of the magnified mode shape.

For additional literature on the image processing aspects of the introduced methodology, the reader is referred to [52,55,56].

4. Experimental demonstration

To demonstrate the application of the proposed method, a laboratory experiment on a simply supported beam was carried out, followed by an industrial test case (sheet-metal impeller cover of a vacuum-cleaner motor).

4.1. Laboratory experiment

A steel beam with dimensions $l \times w \times h = 500 \times 30 \times 15$ mm was used in the laboratory experiment, see Fig. 4. A 2-mm-wide and 7-mm-deep notch that spanned the entire width of the beam was made on the underside, 250 mm in the x direction. The beam was placed on foam pads to simulate a free-free supported state.

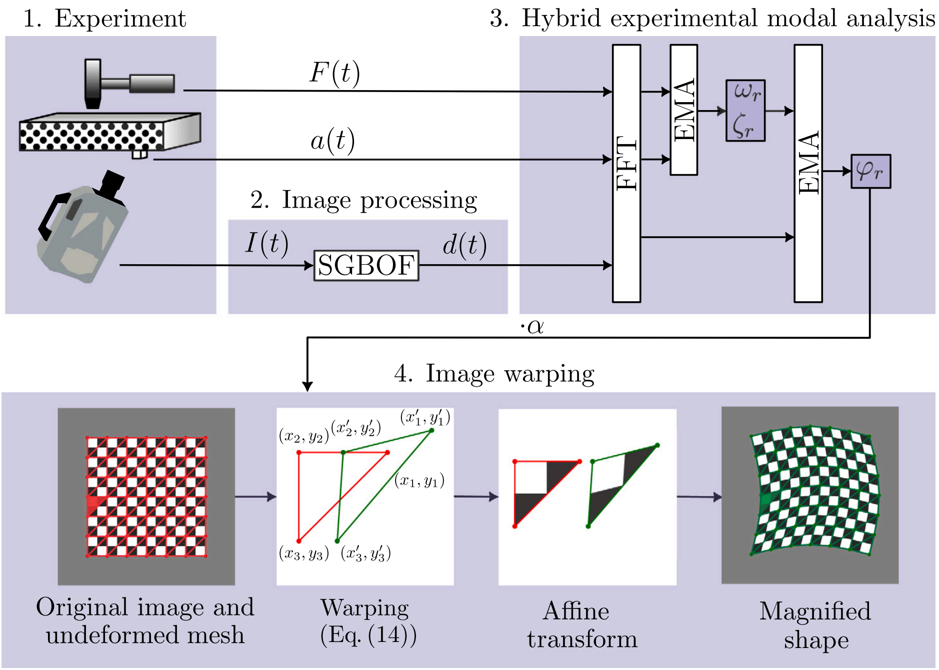

Fig. 3. Block diagram of the introduced method: 1. Experiment, 2. Image processing using the simplified gradient-based optical flow (SGBOF) method, 3. Hybrid experimental modal analysis (EMA) and 4. Image warping to produce an image of the magnified mode shape.

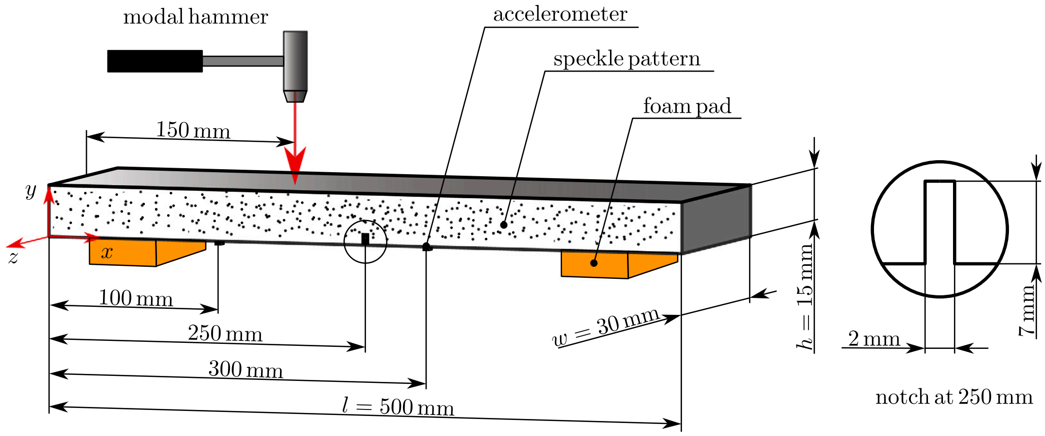

Fig. 4. Schematic of the beam used in the experiment.

A Photron FastCam SA-Z type 2100K-M-64 GB high-speed camera combined with a Sigma lens (focal length 50 mm and f2.8) was used to acquire the full-field displacement data. The camera was placed at a distance of 115 cm and aligned so that only the displacements in the xy plane were measured. A speckle-pattern sticker was applied to the xy plane. The beam was illuminated with two flickerless LED lights and background reflections were mitigated by a black screen, placed behind the beam. Two single-axis piezoelectric accelerometers were attached to the underside of the beam (at 100 and 300 mm along x axis) to measure the response of the beam in the y direction (Fig. 4).

The beam was excited using a PCB 086C03 modal impact hammer in the y direction at a single location (100 mm along the x axis). Care was taken to strike the beam in the middle (in direction z) to ensure that the beam responded mostly in the observed xy plane and no torsional or transversal modes were excited in the z direction.

The force and acceleration signals were sampled at 51.2 kHz, while the frame rate of the camera was set to 100 000 frames per second. A high sampling frequency was used to adequately measure the transient response to the impulse excitation. The duration of all measurements was 1 s. As shown in Fig. 6(a), the field-of-view of the recording was set to 1024×72 pixels, also including some background so object segmentation based on Eq. (11) was later used. The quantization of the intensity was 12-bit (4096 discrete intensity levels).

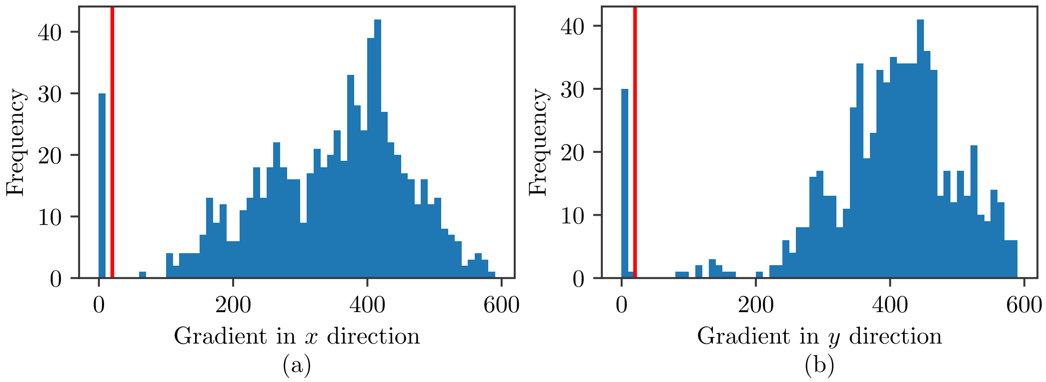

Fig. 5. Histograms of the ninth-largest gradient values from each subset in the (a) x direction and (b) y direction.

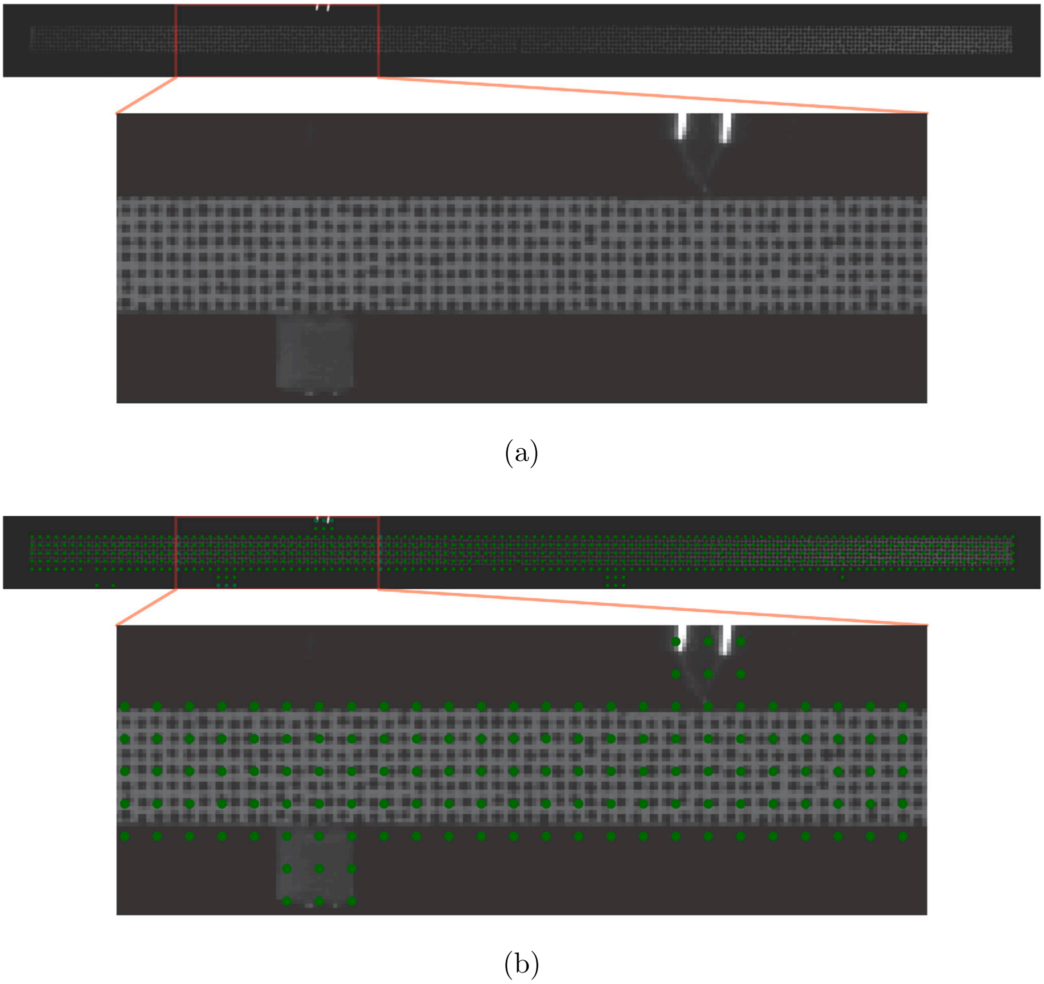

Fig. 6. (a) The reference image I_0 of the simply supported beam. (b) The central pixels of the subsets selected using Eq. (11) and $g_{x,\mathrm{min}} = g_{y,\mathrm{min}} = 10$.

The mode-shape magnification method identifies displacements within selected subsets. In this laboratory experiment, the first 100 images were used to create the reference image I_0 (Eq. (5)), shown in Fig. 6(a). The subset size was set to 7 × 7 pixels and $n_x = n_y = 9$ pixels with the largest intensity gradient in the x and y directions respectively were selected for each subset. The intensity-gradient limit values ($g_{x,\mathrm{min}}, g_{y,\mathrm{min}}$) were determined in the next step. The smallest gradient values in the x and y directions were extracted from among the selected n_x and n_y pixels of each subset and displayed in the histograms in Fig. 5. The background

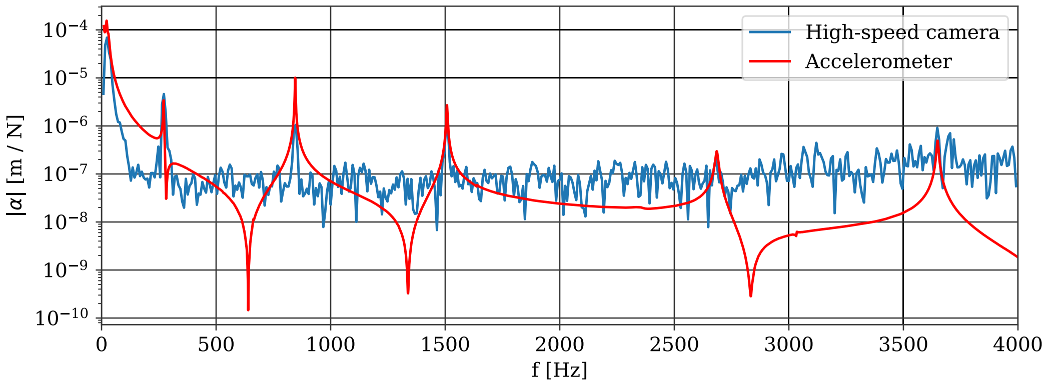

Fig. 7. Comparison of the image and accelerometer based frequency response functions (Freely supported beam experiment).

Table 1
Modal frequencies and corresponding mode-shape scaling factors of the simply supported beam.

r	1	2	3	4	5
f_r [Hz]	270	844	1507	2685	3649
c_r [/]	100	100	200	300	200
Physical scaling fact. [/] $\times 10^3$	1.4	1.4	7.0	39.6	27.5

of the image is represented by bins 0–10 and 10–20 and the gradient limit values ($g_{x,\min}, g_{y,\min}$) were consequently set to 20, as indicated by the red line on both histograms.

In Fig. 6(b) the central pixel of each subset is represented by a green dot. The beam was successfully segmented from the background; however, the tip of the modal hammer, both accelerometers and some areas of the foam pads were manually excluded from further consideration. The displacements were identified using Eq. (3) and the first step of the mode-shape magnification method was concluded with the calculation of the average displacement for each subset, as defined with Eq. (12).

In the second step, the experimental modal analysis using the hybrid method was applied. The FRFs were obtained for both the camera and accelerometer measurements. The H_1 estimator of the high-speed-camera-based FRF produced the best results as it is robust to output signal noise [54]. Averaging in the frequency domain was applied and the displacement time signals were split into 8 segments with 25% overlap and the Hann window was employed. The frequency range from 0 to 4000 Hz was investigated. The obtained image-based FRF is shown in Fig. 7 in comparison with the reference accelerometer FRF. The resonance peaks of the first three modes are clearly visible on both functions, however the fourth and fifth mode can only be identified based on the reference accelerometer measurement.

In the third step of the method, the triangle mesh was created and warped using Eq. (14). Each identified mode shape ($\phi_{x,j,r}, \phi_{y,j,r}$) was considered separately.

In the final step of the mode-shape magnification method the image was warped. For each undeformed mesh element, a rectangular subsection was cropped from the reference image I_0. The rectangular section was defined by the axis-aligned bounding rectangle of the mesh element. After the rectangular image section was transformed (Eq. (9)), the area defined by the corresponding deformed mesh element was masked out and inserted into the output image. Once this process was repeated for all mesh elements, the output image was obtained.

The use of the mode-shape magnification method is demonstrated for the case of the first bending mode shape of the beam in Fig. 8. The central pixels of the considered subsets are represented by green dots in Fig. 8(a). Both components of the observed mode shape ($\phi_{x,j,1}, \phi_{y,j,1}$) are depicted by a vector plot in Fig. 8(b). Next, a triangle mesh is created (Section 2.3) and warped using Eq. (14). The mesh is displayed in Fig. 8(c) in the undeformed (green color) and deformed (red color) states. In Fig. 8(d) the transformed image is displayed with the overlaying deformed mesh and Fig. 8(e) is the final result of the proposed method.

The investigated frequency range included the first 5 bending mode shapes of the beam. Table 1 gives the natural frequencies and mode-shape scaling factors c_r that were used to obtain the motion-magnified images of the first five mode shapes, shown in Fig. 9.

The physical magnification factors were also calculated for each mode shape to determine the actual magnitude of magnification between the measured and magnified displacements. To obtain the physical magnification factor for each mode, the displacements, obtained from the high-speed camera measurement, were transformed to the frequency domain using the Fast Fourier transform (FFT). The obtained spectrum was then amplitude normalized (by the number of samples used). The physical magnification factor was then calculated for each subset separately as the ratio between the magnified mode shape (as shown in Fig. 9) and the value of the amplitude spectrum at the corresponding natural frequency. The average physical magnification factor for each mode shape is presented in Table 1, where magnification of up to 40 thousand times was used. The obtained value represents the ratio between the measured displacement amplitude and the amplitude of the displacement shown in the magnified result (always in pixels).

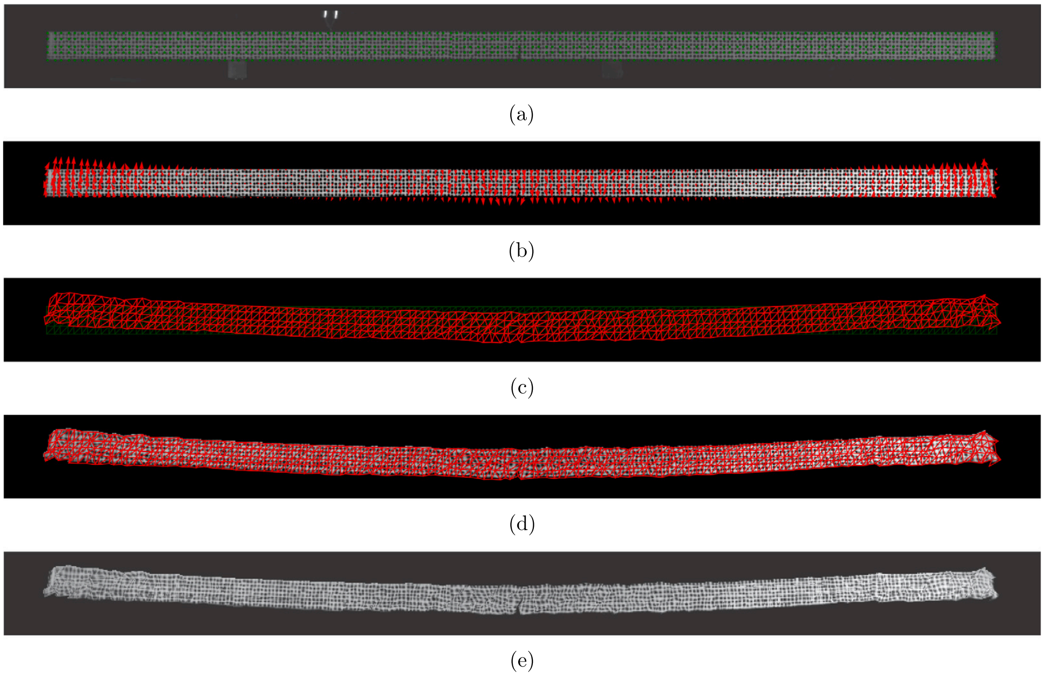

Fig. 8. Proposed method demonstrated for the first modal shape of the beam, (a) The central pixels of the considered subsets, (b) Vector plot representation of the mode shape, (c) The mesh in its original and deformed state, (d) The transformed image with overlayed with the deformed mesh, (e) The final result.

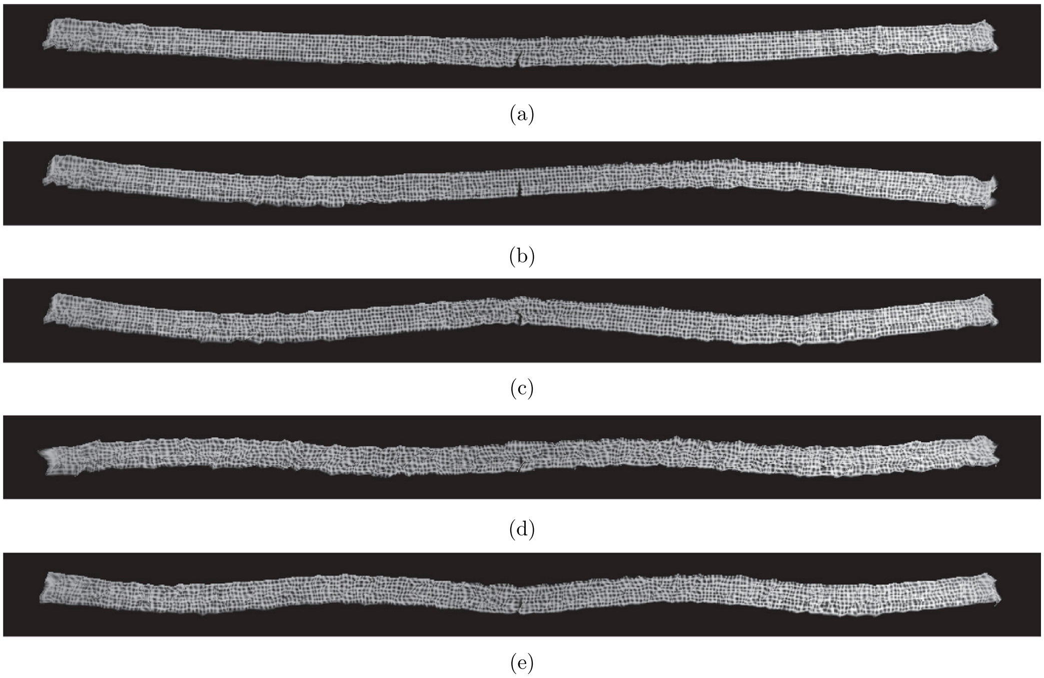

Fig. 9. The first 5 magnified bending mode shapes of the beam, (a) Natural frequency = 270 Hz - 1.4 thousand magnification, (b) 844 Hz, 1.4 thousand magnified, (c) 1507 Hz, 7 thousand magnified, (d) 2685 Hz, 39.6 thousand magnified, (e) 3649 Hz, 27.5 thousand magnified.

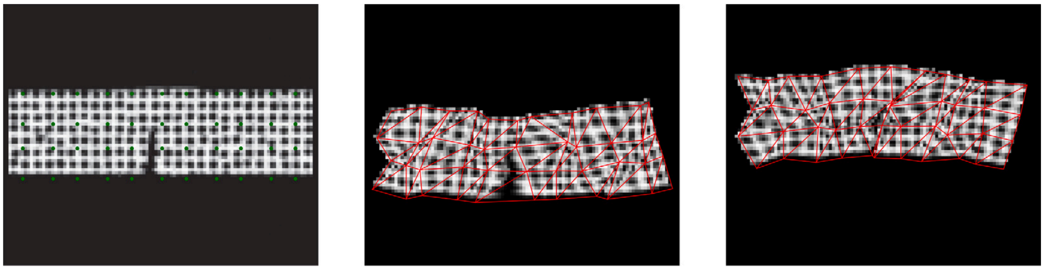
(a) (b) (c)

Fig. 10. Magnified opening and closing of the notch for mode 5.

The modal hammer excitation was performed close to a node of the first (270 Hz) and fourth (2685 Hz) mode shape (at a distance of roughly 30 and 20 mm, respectively). The displacements of the first mode were large enough to still produce a clear shape. For the fourth mode shape, a higher mode-shape scaling factor c_4 was used and more noise is present on the resulting amplified mode shape image in Fig. 9(d) than for the other mode shapes.

To produce the mode-shape-magnified video in the time domain, all elements of the observed mode shape are multiplied by a unitary sine-wave function. For each sample of the sine wave, the mesh and image-warping steps described in Sections 3.3 and 3.4 are repeated and a separate image is created.

Next, the notch on the beam was used to evaluate the performance of the proposed method on local deformations. Video data from the original test was spatially cropped and the range of interest was set to 100 pixels wide and centered on the notch. A column of mesh nodes was aligned to either side of the notch, as seen in Fig. 10(a), while the two boundary deflection states for mode 5 are depicted in Fig. 10(b) and (c). The oscillation causes the notch to open and close, as it is located on an anti-node of the mode shape.

In the notch, the amplitude of displacement is in the range of $0.1\ \mu\mathrm{m}$ (see Fig. 13 in Appendix A) and well below the noise floor of the high-speed camera measurement and some artifacts are consequently present. Due to the employment of the hybrid modal identification approach however, coherent motion could still be extracted and visualized even in the case of high-frequency, small displacement vibrations (see also the supplementing video).

4.2. Industrial test case: Impeller cover

A sheet-metal impeller cover of a vacuum-cleaner motor with a diameter of 130 mm was used to evaluate the performance of the proposed method in the case of a more complex geometry and modal shapes.

This time a small electromagnetic shaker was used to excite the structure with a random signal. The shaker was supported from the ceiling by string and orientated vertically downward. A PCB 208C01 force sensor was glued to the impeller cover radially and attached to the shaker via a stinger. A Dytran 3224 series accelerometer was glued to the inside of the cover.

A speckle pattern was applied to the outer surface of the cover. A Nikon lens (focal length 105 mm and f2.8) was fitted to the high-speed camera. The camera was positioned at a distance of roughly 150 cm and at an angle of roughly 45° relative to the axis of the impeller cover, so that neither the front or the side face of the cover were aligned with the camera's imaging plane. The larger focal length and greater relative distance were used to create a larger depth of field of the video, so that the entire object was in focus (see Fig. 11).

The field-of-view was set to 640×584 pixels, while the grayscale depth was 12-bit. The sampling frequency of 10 000 fps was used for the 4 s measurement. The excitation was stationary and Gaussian random in the frequency range from 50 to 5000 Hz.

In the subset selection step the subset size was set to 25×25 pixels, and $n_x = n_y = 11$ pixels were chosen for each subset. The gradient limits (11) were set to 100 based on the histogram procedure, explained in Section 4.1. The hybrid method experimental modal analysis 2.2 was performed in the frequency range up to 2000 Hz and 11 natural modes were found.

The result for the third identified mode shape is depicted in Fig. 12 in the form of three frames of the mode-shape-magnified video. The corresponding modal frequency is 353 Hz and the mode displacements were amplified by a mode-shape scaling factor of 40 (physical scaling factor: 10^4).

The amplified mode shape of the impeller cover is better represented in the video as part of the supplementary material of this article.

5. Conclusion

In this research, a mode-shape magnification method is introduced as an alternative to existing motion-magnification methods. Full-field displacements are obtained from image data (e.g. by using the simplified 2D gradient-based optical flow method). To identify mode shapes covered in noise at the sub-pixel range, hybrid experimental modal analysis is applied (identification of poles

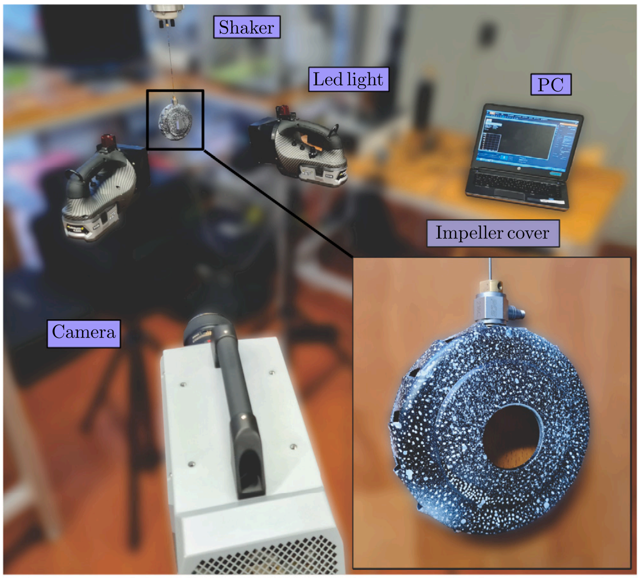

Fig. 11. Experimental setup with high-speed camera and impeller cover.

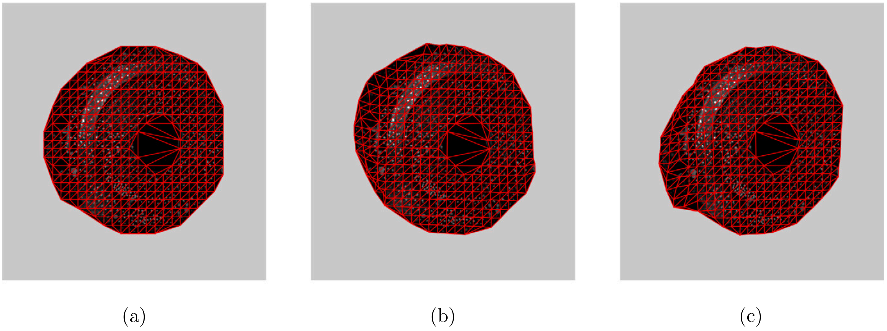
(a) (b) (c)

Fig. 12. Oscillation of the third identified mode shape of the cover, magnified by a mode-shape scaling factor of 40 and shown at three time steps, (a) Mode shape at time 0, (b) Mode shape at 1/3 of the oscillation period, (c) Mode shape at 2/3 of the oscillation period.

is done using a high-dynamic range sensor, like piezoelectric accelerometer). To perform the mode-shape magnification, a planar triangle mesh is formed on top of the image data; the mesh is then warped in accordance with the identified mode shape. For each mesh element, an affine transformation matrix is calculated based on the known locations of the nodes in the original and warped meshes. Mesh-element-wise affine transformation is then performed and the transformed elements are assembled to produce the magnified image of the mode shape.

The proposed mode-shape magnification method is based on the hybrid experimental modal analysis [4], extended to two dimensions in this manuscript. This enables the extraction and visualization of motion completely covered by image noise. In addition, a linear relationship to image intensity values is used to extract displacement data only from the most appropriate pixels (selected based on the image intensity gradient). Consequently, the proposed method is computationally significantly less intensive, compared to existing motion magnification methods.

The application of the proposed method was first demonstrated on a laboratory test case of a simply supported notched beam, excited using an impact via modal hammer. The frequency range up to 4000 Hz was examined and the first five bending modes of the beam were identified. The mode shapes were physically amplified by factors up to 40 thousand times: clear magnified images of all five mode shapes were obtained. Additionally, the performance of the proposed method near local details was demonstrated by examining a small notch on the beam. The opening and closing of the notch during the oscillations was successfully identified and magnified.

The second experiment was performed on a real industrial product: a sheet-metal impeller cover of a vacuum-cleaner suction unit. Even though the test specimen presented a complex geometry that exhibited a 3D dynamic response, modes up to 2 kHz were successfully identified and visualized using the proposed method based on a single-camera 2D displacement-identification approach.

The proposed method is relatively easily applied to real industrial cases and was shown to provide magnification factors up to 40 thousand times.

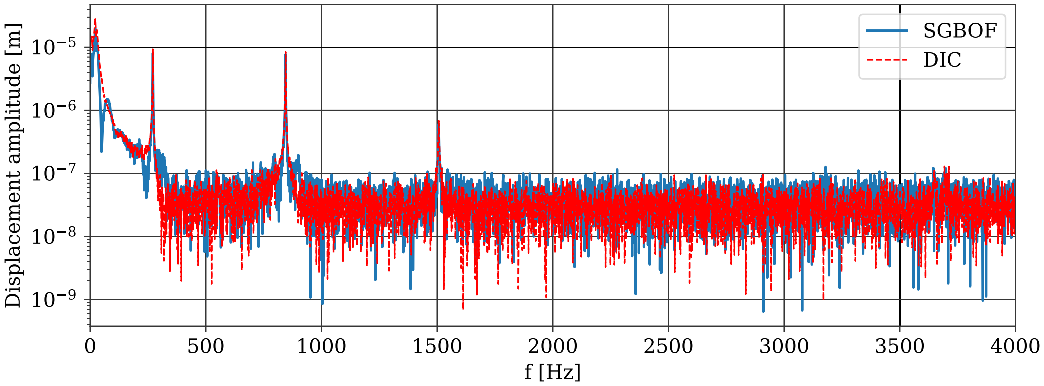

Fig. 13. Comparison of the amplitude spectra of a single subset obtained by the extended simplified gradient-based optical flow (SGBOF) method and DIC.

CRediT authorship contribution statement

Krištof Čufar: Data curation, Formal analysis, Investigation, Methodology, Software, Validation, Visualization, Writing – original draft, Writing – review & editing. **Janko Slavič:** Conceptualization, Funding acquisition, Investigation, Methodology, Project administration, Resources, Software, Supervision, Validation, Writing – review & editing. **Miha Boltežar:** Conceptualization, Funding acquisition, Investigation, Resources, Validation, Writing – review & editing.

Declaration of competing interest

The authors declare that they have no known competing financial interests or personal relationships that could have appeared to influence the work reported in this paper.

Data availability

Data will be made available on request.

Acknowledgments

The authors acknowledge partial financial support from the Slovenian Research Agency, Slovenia (research core funding No. P2-0263 and research project N2-0144).

Appendix A. Comments on using DIC

In the following a comment is provided regarding why the simplified gradient-based optical flow approach is proposed instead of the better established Digital Image Correlation (DIC). Displacements are identified using a linear relationship to the image intensity values, which makes their calculation considerably faster than with the (possibly iterative) correlation approach of DIC [3]. Additionally, displacements are only identified in a selection of pixels with the highest intensity gradients within a subset, which further shortens the computational time. Since the observed displacements are expected to be in the sub-pixel range, only the translation of the subset is of interest and the rotation and deformation are expected to be negligible.

A comparison of the proposed approach with DIC was performed for the case of the freely supported beam. An open-source python implementation of the Lucas-Kanade algorithm was used [53]. As with the described approach, subsets of 7×7 pixels were also used for the DIC computation.

The computation time of the proposed methodology was significantly shorter (152 s compared to 332 min for DIC), while the accuracy of the motion estimation was only slightly better in the case of DIC. The resulting amplitude spectra of a single subset (driving point) are shown in Fig. 13 where the slightly lower noise floor of DIC is evident. Only the vertical component of displacement was considered here.

In the case of both methods, the first three resonance peaks are visible, while the fourth and fifth mode are covered in noise. These modes can only be extracted using a supplementary accelerometer measurement and the hybrid modal identification method.

Appendix B. Comparison to phase-based motion magnification

To highlight the benefits of the introduced mode-shape magnification method, a comparison with the established phase-based motion magnification approach [26] was also performed using an open-source python implementation [57]. The original implementation was extended with an alternative radial windowing function, introduced in the Appendix of [26] and the spatial smoothing of the phase signals [26].

The comparison between the introduced mode-shape magnification method and the phase-based motion magnification was performed for the case of the impeller cover mode at 353 Hz, presented above. The phase-based approach considers motion in every pixel of the input video and is consequently very intensive. To manage the amount of data, the original recording of 4 s at 10 thousand FPS (frames per second) was decimated by a factor of 10 and truncated to 1000 images, resulting in a 1 s long video with the effective recording rate of 1000 FPS.

Sub-octave filtering (4 band-pass filters for each pyramid layer) was also employed to allow for higher achievable magnification factors along with the alternative radial windowing function [26]. The number of orientation bands was set to 2, to correspond to the introduced mode-shape magnification method, where only displacements in the x and y directions are considered.

The highest magnification factor, achieved by the phase-based approach was 400 (compared with the physical scaling factor of 10^4, achieved by the introduced method). Higher magnification factors lead to significant deteriorations of image quality. The phase-based approach was not successful at higher frequencies of vibrations (with lower amplitudes of displacement); while the introduced method had no problems identifying and visualizing further 8 modes.

To provide a fair comparison of the efficiency of the introduced and phase-based motion magnification methods, the computational times were normalized by the amount of input data (number of pixel intensity values used in the computation). The newly introduced mode-shape magnification method achieved a computation time of 0.60 s/million pixels values, while the phase-based approach achieved a time of 7.19 s/million pixel values. Consequently, the introduced method was 12.1 times faster for the described example.

The result of the described application of phase-based motion magnification is given in the supplementary material of the manuscript.

Appendix C. Supplementary data

Supplementary material related to this article can be found online at https://doi.org/10.1016/j.ymssp.2024.111336.

References

[1] C. Warren, C. Niezrecki, P. Avitabile, P. Pingle, Comparison of FRF measurements and mode shapes determined using optically image based, laser, and accelerometer measurements, Mech. Syst. Signal Process. 25 (2011) 2191–2202, http://dx.doi.org/10.1016/j.ymssp.2011.01.018.

[2] P.L. Reu, D.P. Rohe, L.D. Jacobs, Comparison of DIC and LDV for practical vibration and modal measurements, Mech. Syst. Signal Process. 86 (2017) 2–16, http://dx.doi.org/10.1016/j.ymssp.2016.02.006.

[3] J. Javh, J. Slavič, M. Boltežar, The subpixel resolution of optical-flow-based modal analysis, Mech. Syst. Signal Process. 88 (2017) 89–99, http://dx.doi.org/10.1016/j.ymssp.2016.11.009.

[4] J. Javh, J. Slavič, M. Boltežar, High frequency modal identification on noisy high-speed camera data, Mech. Syst. Signal Process. 98 (2018) 344–351, http://dx.doi.org/10.1016/j.ymssp.2017.05.008.

[5] J.G. Chen, N. Wadhwa, Y.J. Cha, F. Durand, W.T. Freeman, O. Buyukozturk, Modal identification of simple structures with high-speed video using motion magnification, J. Sound Vib. 345 (2015) 58–71, http://dx.doi.org/10.1016/j.jsv.2015.01.024.

[6] N.A. Valente, C.T. do Cabo, Z. Mao, C. Niezrecki, Quantification of phase-based magnified motion using image enhancement and optical flow techniques, Measurement 189 (2022) 110508, http://dx.doi.org/10.1016/j.measurement.2021.110508.

[7] P. Olaszek, Investigation of the dynamic characteristic of bridge structures using a computer vision method, Measurement 25 (1999) 227–236, http://dx.doi.org/10.1016/S0263-2241(99)00006-8.

[8] T.G. Ryall, C.S. Fraser, Determination of structural modes of vibration using digital photogrammetry, J. Aircr. 39 (2002) 114–119, http://dx.doi.org/10.2514/2.2903.

[9] T. Siebert, R. Wood, K. Splitthof, High speed image correlation for vibration analysis, J. Phys. Conf. Ser. 181 (2009) 012064, http://dx.doi.org/10.1088/1742-6596/181/1/012064.

[10] M.N. Helfrick, C. Niezrecki, P. Avitabile, T. Schmidt, 3D digital image correlation methods for full-field vibration measurement, Mech. Syst. Signal Process. 25 (2011) 917–927, http://dx.doi.org/10.1016/j.ymssp.2010.08.013.

[11] T.J. Beberniss, D.A. Ehrhardt, High-speed 3D digital image correlation vibration measurement: Recent advancements and noted limitations, Mech. Syst. Signal Process. 86 (2017) 35–48, http://dx.doi.org/10.1016/j.ymssp.2016.04.014.

[12] J. Baqersad, P. Poozesh, C. Niezrecki, P. Avitabile, Photogrammetry and optical methods in structural dynamics – A review, Mech. Syst. Signal Process. 86 (2017) 17–34, http://dx.doi.org/10.1016/j.ymssp.2016.02.011.

[13] B.D. Lucas, T. Kanade, An iterative image registration technique with an application to stereo vision, in: 7th International Joint Conference on Artificial Intelligence, Kaufmann Publishers Inc., San Francisco, CA, USA, 1981, pp. 674–679.

[14] J. Javh, J. Slavič, M. Boltežar, Measuring full-field displacement spectral components using photographs taken with a DSLR camera via an analogue Fourier integral, Mech. Syst. Signal Process. 100 (2018) 17–27, http://dx.doi.org/10.1016/j.ymssp.2017.07.024.

[15] D. Gorjup, J. Slavič, M. Boltežar, Frequency domain triangulation for full-field 3D operating-deflection-shape identification, Mech. Syst. Signal Process. 133 (2019) 106287, http://dx.doi.org/10.1016/j.ymssp.2019.106287.

[16] A. Khadka, B. Fick, A. Afshar, M. Tavakoli, J. Baqersad, Non-contact vibration monitoring of rotating wind turbines using a semi-autonomous UAV, Mech. Syst. Signal Process. 138 (2020) http://dx.doi.org/10.1016/j.ymssp.2019.106446.

[17] P. Gardonio, G. Guernieri, E. Turco, L.D. Bo, R. Rinaldo, A. Fusiello, Reconstruction of the sound radiation field from flexural vibration measurements with multiple cameras, Mech. Syst. Signal Process. 195 (2023) 110289, http://dx.doi.org/10.1016/j.ymssp.2023.110289.

[18] H. Hu, J. Wang, C.Z. Dong, J. Chen, T. Wang, A hybrid method for damage detection and condition assessment of hinge joints in hollow slab bridges using physical models and vision-based measurements, Mech. Syst. Signal Process. 183 (2023) 109631, http://dx.doi.org/10.1016/j.ymssp.2022.109631.

[19] S.R. Atashipour, J. Baqersad, Noninvasive identification of directionally-dependent elastic properties of soft tissues using full-field optical data, J. Mech. Behav. Biomed. Mater. (2023) 106266, http://dx.doi.org/10.1016/j.jmbbm.2023.106266.

[20] A. Sarrafi, Z. Mao, C. Niezrecki, P. Poozesh, Vibration-based damage detection in wind turbine blades using Phase-based Motion Estimation and motion magnification, J. Sound Vib. 421 (2018) 300–318, http://dx.doi.org/10.1016/j.jsv.2018.01.050.

[21] G. Liu, M.Z. Li, Z. Mao, Q.S. Yang, Structural motion estimation via Hilbert transform enhanced phase-based video processing, Mech. Syst. Signal Process. 166 (2022) 108418, http://dx.doi.org/10.1016/j.ymssp.2021.108418.

[22] B. Merainani, B. Xiong, V. Baltazart, M. Döhler, J. Dumoulin, Q. Zhang, Subspace-based modal identification and uncertainty quantification from video image flows, J. Sound Vib. 569 (2024) http://dx.doi.org/10.1016/j.jsv.2023.117957.

[23] C. Liu, A. Torralba, W.T. Freeman, F. Durand, E.H. Adelson, Motion magnification, ACM Trans. Graph. 24 (2005) 519–526, http://dx.doi.org/10.1145/1073204.1073223.

[24] J. Wang, S.M. Drucker, M. Agrawala, M.F. Cohen, The cartoon animation filter, ACM Trans. Graph. 25 (2006) 1169–1173, http://dx.doi.org/10.1145/1179352.1142010.

[25] H.-Y. Wu, M. Rubinstein, E. Shih, J. Guttag, F. Durand, W.T. Freeman, Eulerian video magnification for revealing subtle changes in the world, ACM Trans. Graph. 31 (2012) 1–8, http://dx.doi.org/10.1145/2185520.2185561.

[26] N. Wadhwa, M. Rubinstein, F. Durand, W.T. Freeman, Phase-based video motion processing, ACM Trans. Graph. 32 (2013) 1–10, http://dx.doi.org/10.1145/2461912.2461966.

[27] A.J. Molina-Viedma, L. Felipe-Sesé, E. López-Alba, F. Díaz, High frequency mode shapes characterisation using Digital Image Correlation and phase-based motion magnification, Mech. Syst. Signal Process. 102 (2018) 245–261, http://dx.doi.org/10.1016/j.ymssp.2017.09.019.

[28] P. Poozesh, A. Sarrafi, Z. Mao, P. Avitabile, C. Niezrecki, Feasibility of extracting operating shapes using phase-based motion magnification technique and stereo-photogrammetry, J. Sound Vib. 407 (2017) 350–366, http://dx.doi.org/10.1016/j.jsv.2017.06.003.

[29] N.A. Valente, A. Sarrafi, Z. Mao, C. Niezrecki, Streamlined particle filtering of phase-based magnified videos for quantified operational deflection shapes, Mech. Syst. Signal Process. 177 (2022) http://dx.doi.org/10.1016/j.ymssp.2022.109233.

[30] F. Cosco, J. Cuenca, W. Desmet, K. Janssens, D. Mundo, Towards phase-based defect detection: A feasibility study in vibrating panels, J. Sound Vib. 537 (2022) 117196, http://dx.doi.org/10.1016/j.jsv.2022.117196.

[31] K. Luo, X. Kong, X. Wang, T. Jiang, G.T. Frøseth, A. Rønnquist, Cable vibration measurement based on broad-band phase-based motion magnification and line tracking algorithm, Mech. Syst. Signal Process. 200 (2023) 110575, http://dx.doi.org/10.1016/j.ymssp.2023.110575.

[32] W. Wang, J.E. Mottershead, T. Siebert, A. Pipino, Frequency response functions of shape features from full-field vibration measurements using digital image correlation, Mech. Syst. Signal Process. 28 (2012) 333–347, http://dx.doi.org/10.1016/j.ymssp.2011.11.023.

[33] Y. Yang, C. Dorn, T. Mancini, Z. Talken, G. Kenyon, C. Farrar, D. Mascareñas, Blind identification of full-field vibration modes from video measurements with phase-based video motion magnification, Mech. Syst. Signal Process. 85 (2017) 567–590, http://dx.doi.org/10.1016/j.ymssp.2016.08.041.

[34] T. Bregar, K. Zaletelj, G. Čepon, J. Slavič, M. Boltežar, Full-field FRF estimation from noisy high-speed-camera data using a dynamic substructuring approach, Mech. Syst. Signal Process. 150 (2021) 107263, http://dx.doi.org/10.1016/j.ymssp.2020.107263.

[35] Y. Wang, F.S. Egner, T. Willems, M. Kirchner, W. Desmet, Camera-based experimental modal analysis with impact excitation: Reaching high frequencies thanks to one accelerometer and random sampling in time, Mech. Syst. Signal Process. 170 (2022) 108879, http://dx.doi.org/10.1016/j.ymssp.2022.108879.

[36] P. Guillaume, P. Verboven, S. Vanlanduit, H.V.D. Auweraer, B. Peeters, A poly-reference implementation of the least-squares complex frequency-domain estimator, in: Proceedings of IMAC, Vol. 21, Society for Experimental Mechanics, Kissimmee, FL, 2003.

[37] I. Tomac, J. Slavič, Damping identification based on a high-speed camera, Mech. Syst. Signal Process. 166 (2022) 108485, http://dx.doi.org/10.1016/j.ymssp.2021.108485.

[38] S. Cao, H. Nian, J. Yan, Z. Lu, C. Xu, Modal analysis and damage localization in plate-type structures via TDD and PE methods based on the data of an integrated highspeed camera system, Mech. Syst. Signal Process. 178 (2022) 109309, http://dx.doi.org/10.1016/j.ymssp.2022.109309.

[39] T. Willems, F.S. Egner, Y. Wang, M. Kirchner, W. Desmet, F. Naets, Time-domain model identification of structural dynamics from spatially dense 3D vision-based measurements, Mech. Syst. Signal Process. 182 (2023) 109553, http://dx.doi.org/10.1016/j.ymssp.2022.109553.

[40] S.L. Feudo, J.L. Dion, F. Renaud, G. Kerschen, J.P. Noël, Video analysis of nonlinear systems with extended Kalman filtering for modal identification, Nonlinear Dynam. 111 (2023) 13263–13277, http://dx.doi.org/10.1007/s11071-023-08560-1.

[41] B.K.P. Horn, B.G. Schunck, Determining optical flow, Artificial Intelligence 17 (1981) 185–203, http://dx.doi.org/10.1016/0004-3702(81)90024-2.

[42] K. Zaletelj, J. Slavič, M. Boltežar, Full-field DIC-based model updating for localized parameter identification, Mech. Syst. Signal Process. 164 (2022) 108287, http://dx.doi.org/10.1016/j.ymssp.2021.108287.

[43] P. Guillaume, S. Vanlanduit, P. Verboven, Frequency domain maximum likelihood identification of modal parameters with confidence intervals, in: Proceedings of ISMA 23, 1998, pp. 16–18.

[44] T. Kailath, Linear Systems, first ed., Prentice-Hall, Inc., Englewood Cliffs, N.J., 1980.

[45] H.V.D. Auweraer, W. Leurs, P. Mas, L. Hermans, Modal parameter estimation from inconsistent data sets, Proc. SPIE - Int. Soc. Opt. Eng. 4062 (2000).

[46] S.J. Owen, A survey of unstructured mesh generation technology, in: 7th International Meshing Roundtable Conference, 2000.

[47] B. Delaunay, Sur la sphere vide. A la memoire de Georges Voronoi, Bull. Acad. Sci. URSS Cl. Sci. Math. (1934) 793–800.

[48] M.D. Berg, O. Cheong, M.V. Kreveld, M. Overmars, Computational Geometry: Algorithms and Applications, Springer Berlin Heidelberg, 2008, pp. 1–386, http://dx.doi.org/10.1007/978-3-540-77974-2.

[49] L.J. Guibas, D.E. Knuth, M. Sharir, Randomized incremental construction of Delaunay and Voronoi diagrams 1, Algorithmica 7 (1992) 381–413.

[50] W. Schroeder, K. Martin, B. Lorensen, The Visualization Toolkit, fourth ed., 2006.

[51] C. Sullivan, A. Kaszynski, PyVista: 3D plotting and mesh analysis through a streamlined interface for the Visualization Toolkit (VTK), J. Open Source Softw. 4 (2019) 1450, http://dx.doi.org/10.21105/joss.01450.

[52] R.C. Gonzalez, R.E.R.E. Woods, Digital Image Processing, fourth ed., Pearson Education Limited, Harlow, 2018.

[53] K. Zaletelj, D. Gorjup, J. Slavič, ladisk/pyidi: Release of the version v.027, 2023.

[54] N.M.M. Maia, J.M.M. Silva, Theoretical and Experimental Modal Analysis, Research Studies Press, Baldock, United Kingdom, 1997.

[55] R. Szeliski, Computer Vision: Algorithms and Applications, first ed., Springer London, London, 2010.

[56] M. Pharr, W. Jakob, G. Humphreys, Physically Based Rendering: From Theory to Implementation, third ed., Elsevier Inc., 2016.

[57] R. Xian, phase-video, 2019, https://github.com/rxian/phase-video.